

Experimental comparison of a wind-turbine and of an actuator-disc near wake

L. E. M. Lignarolo, D. Ragni, C. J. Ferreira, and G. J. W. van Bussel

Citation: *Journal of Renewable and Sustainable Energy* **8**, 023301 (2016); doi: 10.1063/1.4941926

View online: <http://dx.doi.org/10.1063/1.4941926>

View Table of Contents: <http://scitation.aip.org/content/aip/journal/jrse/8/2?ver=pdfcov>

Published by the [AIP Publishing](#)

Articles you may be interested in

[Structure functions, scaling exponents and intermittency in the wake of a wind turbine array](#)

J. Renewable Sustainable Energy **8**, 013304 (2016); 10.1063/1.4941782

[On the statistics of wind turbine wake meandering: An experimental investigation](#)

Phys. Fluids **27**, 075103 (2015); 10.1063/1.4923334

[Effects of energetic coherent motions on the power and wake of an axial-flow turbine](#)

Phys. Fluids **27**, 055104 (2015); 10.1063/1.4921264

[The interaction of helical tip and root vortices in a wind turbine wake](#)

Phys. Fluids **25**, 117102 (2013); 10.1063/1.4824734

[Longitudinal and spanwise vortical structures in a turbulent near wake](#)

Phys. Fluids **12**, 2954 (2000); 10.1063/1.1309532

The logo for AIP APL Photonics. It features the letters 'AIP' in a large, white, sans-serif font on the left. To its right is a vertical yellow bar, followed by the text 'APL Photonics' in a smaller, white, sans-serif font. The background is a vibrant red with a bright yellow sunburst effect emanating from the top right corner.

APL Photonics is pleased to announce
Benjamin Eggleton as its Editor-in-Chief





Experimental comparison of a wind-turbine and of an actuator-disc near wake

L. E. M. Lignarolo,^{a)} D. Ragni, C. J. Ferreira, and G. J. W. van Bussel
*Faculty of Aerospace Engineering, Delft University of Technology, Kluyverweg 1,
 2629 HS Delft, The Netherlands*

(Received 6 August 2015; accepted 16 January 2016; published online 1 March 2016)

The actuator disc (AD) model is commonly used to simplify the simulation of horizontal-axis wind-turbine aerodynamics. The limitations of this approach in reproducing the wake losses in wind farm simulations have been proven by a previous research. The present study is aimed at providing an experimental analysis of the near-wake turbulent flow of a wind turbine (WT) and a porous disc, emulating the actuator disc numerical model. The general purpose is to highlight the similarities and to quantify the differences of the two models in the near-wake region, characterised by the largest discrepancies. The velocity fields in the wake of a wind turbine model and a porous disc (emulation of the actuator disc numerical model) have been measured in a wind tunnel using stereo particle image velocimetry. The study has been conducted at low turbulence intensity in order to separate the problems of the flow mixing caused by the external turbulence and the one caused by the turbulence induced directly by the AD or the WT presence. The analysis, as such, showed the intrinsic differences and similarities between the flows in the two wakes, solely due to the wake-induced flow, with no influence of external flow fluctuations. The data analysis provided the time-average three-component velocity and turbulence intensity fields, pressure fields, rotor and disc loading, vorticity fields, stagnation enthalpy distribution, and mean-flow kinetic-energy fluxes in the shear layer at the border of the wake. The properties have been compared in the wakes of the two models. Even in the absence of turbulence, the results show a good match in the thrust and energy coefficient, velocity, pressure, and enthalpy fields between wind turbine and actuator disc. However, the results show a different turbulence intensity and turbulent mixing. The results suggest the possibility to extend the use of the actuator disc model in numerical simulation until the very near wake, provided that the turbulent mixing is correctly represented. © 2016 AIP Publishing LLC. [<http://dx.doi.org/10.1063/1.4941926>]

NOMENCLATURE

a	induction factor
A	area
AD	actuator disc
c	blade chord
C_D	drag coefficient
c_p	pressure coefficient
C_t	thrust coefficient
c_p^+ and c_p^-	upwind and downwind pressure coefficients
D	diameter
DR	digital resolution
e	internal energy per unit mass

^{a)}E-mail: l.lignarolo@tudelft.nl

\dot{E}	internal energy variation per unit time
FOV	field of view
h	enthalpy per unit mass
H_∞	free stream enthalpy per unit mass
I_w	interrogation window size
K_E	mean-flow average kinetic energy
\dot{m}	mass flow rate
$N\#$	number of vectors
OJF	open jet facility
p	pressure
POD	proper orthogonal decomposition
q	flow kinetic energy per unit mass
r	blade radial location
R	radius
Re_D	diameter-based Reynolds number
Re_{cr}	chord-based Reynolds number at the root
Re_{ct}	chord-based Reynolds number at the tip
S	vector spacing
SPIV	stereoscopic particle image velocimetry
t	time
TI_i	turbulence intensity in the i -direction
TI_∞	free stream turbulence intensity
u_i and u_j	velocity in the i - and j -direction
U_∞	free stream velocity
u_{RMS}	RMS velocity
$u'v'$	Reynolds stresses in the x - y plane
u'_i and u'_j	velocity fluctuation in the i - and j -direction
$u'_i u'_j$	Reynolds stresses in the i - j plane
\dot{W}	mechanical power
WT	wind turbine
x,y,z	axial, radial and azimuthal direction
δ	mesh spacing
Δ	variation
λ	tip-speed ratio
μ	dynamic viscosity
v	angular speed
ζ	porosity
ρ	density
Φ	mean-flow kinetic-energy flux
ω	vorticity
...	time average quantity

I. INTRODUCTION

Currently in-use, wind farm numerical models often struggle to accurately reproduce the flow within a wind farm, in particular, at the second row of wind turbines (WT) as the incoming flow develops from an atmospheric boundary layer to a wind farm canopy boundary layer. For this reason, the wind energy community is working toward full-wake models, including a better representation of the near-wake flow induced by a more realistic modelling of rotor aerodynamics (Sanz Rodrigo and Moriarty, 2014). The actuator disc (AD) is a thin circular region where body forces extract momentum from the flow: it is commonly used for modelling the rotor of a horizontal axis wind turbine for simplifying the numerical simulation of the flow development in a wind farm. This simplification is obtained at the expenses of accuracy in the near wake, which is strongly affected by the presence of the rotating blades (Lignarolo *et al.*, 2014b), whereas in

the far wake this simplification is generally more acceptable (see the numerical analysis by [Wu and Porté-Agel \(2011\)](#) on the far-wake discrepancies in the flow prediction between a wind turbine and an actuator disc). [Schepers \(2012\)](#) noted that the actuator disc approach, in combination with the k - ε turbulence model, leads to strong velocity gradients at the wake edges, causing unphysical turbulence production peaks, which enhance the near-wake mixing. In his review study, he suggested that the actuator disc approach often fails in reproducing the effects of flow turbulence, due to the absence of the blade tip-vortex development and breakdown and writes about the importance of investigating how to reduce the inaccuracy of the AD model in the wake region within 5 diameters from the rotor. In fact, the incorrect estimation of the near wake turbulence has repercussions on the mixing process across the wake and ultimately on the rate at which the wake recovers flow momentum is incorrectly modelled ([Lignarolo *et al.*, 2014b](#) and [Schepers, 2012](#)). With the increased utilization of the wind-farm space, this limitation is no longer acceptable for current engineering applications. For example, in the Lillgrud off-shore wind farm, rotors are dislocated in grid with spacing between 3.3 and 4.3 diameters ([Gaumond *et al.*, 2012](#)), and in the Horns Rev off-shore wind farm around 7 diameters ([Barthelmie *et al.*, 2007](#)).

Recent extensive application of the actuator disc model in the numerical simulation of wind farms can be found in the works of [Meyers and Meneveau \(2012\)](#) and [Calaf *et al.* \(2010\)](#). [El Kasmi and Masson \(2008\)](#) developed a modified k - ε model for the actuator disc accounting for energy exchange between large and small scale turbulence structures in the region close to the disc. [Nishino and Willden \(2012\)](#) studied numerically the effect of the near wake mixing on the energy extraction performance of a wind turbine simulated with the actuator disc model. Other examples of actuator disc application in numerical simulations can be found in the thesis of [Mikkelsen \(2003\)](#) and in the reviews from [Sandse *et al.* \(2011\)](#), [Schepers \(2012\)](#), and [Vermeer *et al.* \(2003\)](#). Despite the popularity of this simplified numerical model, too seldom this has been taken into consideration for wind tunnel studies. The actuator disc can be emulated in a wind tunnel by a porous disc. The device, which can be realised with different techniques, does not extract directly energy from the flow, but has the function to dissipate the kinetic energy of the incoming wind into turbulence and, eventually, into heat. Few studies are available, which analyse the flow field in the near wake of a porous disc with the purpose of emulating a wind turbine wake and examples of various techniques for realising the model can be found. For instance, [Aubrun *et al.* \(2013\)](#) and [Aubrun *et al.* \(2007\)](#) manufactured a small-scale porous disc using fine metal meshes, while perforated metal plates have been adopted by [Medici \(2005\)](#) and [Sforza *et al.* \(1981\)](#). [Pierella and Sætran \(2010\)](#) realised a porous disc with wooden grids. Nevertheless, in a direct experimental comparison of the turbulent flow in the near wake, a porous disc with the one of the rotating turbines of the same dimension and axial force, with high-resolution 2D measurements, is currently not available.

The present study is aimed at providing an experimental analysis of the near-wake turbulent flow of a WT and a porous disc emulating the AD numerical model. The underlying question is how much the near wake of a WT differs from the one of the ADs given similarity of dimension, axial force, and extracted energy. The wake velocity field is measured in the low-speed Open Jet Facility (OJF) wind tunnel of Delft University of Technology (TUDelft) with the stereoscopic particle image velocimetry (SPIV) technique. The porous disc is assembled in order to have the same diameter and drag coefficient of the WT model. The latter is the same two-bladed 60 cm diameter rotor used by [Lignarolo *et al.* \(2014a\)](#). The comparison of the two wakes is conducted in the presence of an instability of the tip-vortex helical structure, the so-called *leapfrogging*, which causes the tip vortices to pair and roll around each other to form a single vortex structure. The tip-vortex instability is in fact a critical near-wake feature, whose main effect is to start a more efficient mixing process which anticipates the far wake features. This phenomenon cannot be reproduced with the AD model and as such constitutes a major difference between the two wakes. A comparison between a WT wake and an AD wake in the presence of leapfrogging is for this reason of particular interest. Following the experimental studies of [Dobrev *et al.* \(2008\)](#), [Felli *et al.* \(2011\)](#), and [Sherry *et al.* \(2010\)](#), [Lignarolo *et al.* \(2014a\)](#) have shown how the instability of the tip-vortex helix has a major effect on the wake

mixing and re-energising mechanism. Lignarolo *et al.* (2015a) have conducted a detailed analysis of the effect on the turbulence field and wake mixing due to the presence of the leapfrogging instability. Bolnot *et al.* (2011) simulated numerically the helical wake using an array of axisymmetric vortex-rings for studying the onset of pair-wise instability in helicopter and wind-unknown_hyphen;turbine rotor wakes. Leweke *et al.* (2013) measured experimentally the growth rate of pair-wise instability in a water channel with different triggering modulations. Ivanell (2009) and Ivanell *et al.* (2010) reproduced with large eddy simulation the tip-vortex helix development and instability and measured the near wake length as a function of the inflow turbulence. In this study, the wake instability was triggered by an artificial disturbance introduced at the blade tip during the simulation. In experimental studies by Bolnot *et al.* (2014) and Odemark and Fransson (2013), artificial disturbances were also used for triggering the tip-vortex instability, as asymmetries in the rotor geometry and pulsed air jets. In the present study, the leapfrogging is triggered by an asymmetry of the blade pitch angle, as by Lignarolo *et al.* (2014a). The use of an adapted formulation of the momentum equation in differential form allowed to compute the pressure field and stagnation enthalpy around the rotor and the porous disc directly from the velocity data in the incompressible regime (Ragni *et al.*, 2011; 2012; and van Oudheusden, 2013). The out-of-plane vorticity field is calculated by differentiation of the time-average velocity field with a central difference scheme. The three-component turbulence intensity is calculated and compared in the wakes of both models. A double decomposition of the flow velocity field is employed to extend the analysis performed by Lignarolo *et al.* (2015b) and to quantify the mean-flow kinetic-energy transport across the wake shear layer. In this regard, two wake locations are chosen before and after the leapfrogging and results are compared with the ones obtained in the wake of the actuator disc at the same locations.

Most of the studies mentioned in this section have been performed in presence of high wind tunnel turbulence or simulated atmospheric boundary layers (and atmospheric turbulence). The present study has been conducted at a very low turbulence intensity (0.5%) in order to focus the analysis solely on the wake-induced flow, with no influence of external flow fluctuation, minimising the number of parameters affecting the wake mixing. The objective is in fact to study the intrinsic differences and similarities between the flow in the wake of an AD and a WT, separating the problems of the mixing caused by the external turbulence and the one caused by the turbulence induced directly by the AD or the WT. The scope is not to represent a real situation, but to analyse the core nature of an AD and a WT wake in its essence. Additionally, the analysis of the wake meandering (Medici, 2005) is not in the scope of the present study and the measurements are not organised for capturing such low-frequency oscillations.

II. EXPERIMENTAL METHOD

The present section contains information on the wind-tunnel and experimental models used in this project. Section II A contains descriptions of the OJF wind-tunnel. The wind turbine model and the porous disc design are presented in Sections II B and II C, respectively. Sections II D and II E summarise the experimental conditions and the SPIV setup parameters. In Section II F, the Reynolds-average mean-flow kinetic energy transport equation is derived.

A. Wind-tunnel

Experiments have been conducted in the OJF wind tunnel located at TUDelft. The OJF is a low-speed closed-loop open-jet wind tunnel with an octagonal test section, having an equivalent diameter of 3 m and a contraction ratio of 3:1. It delivers a uniform stream with about 0.5% turbulent intensity in the region within 1 m distance from the nozzle and lower than 2% until 6 m from the nozzle exit. At the latter distance, the uniform-flow section reduces to approximately $2 \times 2 \text{ m}^2$. A detailed characterization of the wind-tunnel flow can be found by Lignarolo *et al.* (2014a). The flow is driven by a fan with an electrical engine of 500 kW and the temperature is kept constant at 20 °C by a heat exchanger which provides up to 350 kW of cooling power.

B. Wind-turbine model

A two-bladed horizontal-axis wind-turbine with a 0.6 m diameter has been designed and the blades have been manufactured in aluminium with a high-precision CNC milling machine. The Eppler E387 airfoil with 9.06% thickness (Selig *et al.*, 1995) has been used, with a twist distribution from 4.4° at the tip to 19.4° at the root. The maximum blade chord is 0.074 m at $r/R=0.18$, with r being the radial coordinate. The design (optimal) tip-speed ratio was $\lambda = v R/U_\infty = 6$. In the present experiments, the turbine was operated at an above-optimal tip-speed ratio $\lambda = 6.97$ at a free-stream wind speed of $U_\infty = 4.7$ m/s. The rotational speed was $v = 109.3$ rad/s (see Table I). The maximum chord-based Reynolds number achieved at these conditions is $Re_{ct} = 96\,000$ at the blade tip. The diameter-based Reynolds number is $Re_D = 188\,000$, which is about one order of magnitude lower than in full-scale operating conditions. The nacelle was designed for minimising its effect on the flow: the ratio rotor-to-nacelle area is less than 6%. The studies of Whale *et al.* (2000) have demonstrated that the wake exhibits a low dependency on the Reynolds number, comparing experimental measurements in the wake of a small wind-turbine with a chord-based Reynolds number ranging from 6400 to 16 000 with the results from an inviscid vortex code, representative of an infinite Reynolds number. The comparison shows a weak sensitivity to Reynolds number on the fundamental behaviour of the helical vortex wake, because the numerical results are fully comparable with the experimental ones. The study of Chamorro *et al.* (2012) suggest that main flow statistics become independent of Reynolds number from $Re = 9.3 \times 10^4$, lower than the value estimated in the present experiments. The model was installed at 1.17 rotor diameters (0.7 m) from the tunnel exit. The wind-tunnel blockage-ratio is 0.04. As in similar cases in the previous literature, no blockage correction is applied (Chen and Liou, 2011 and Schreck *et al.*, 2007). A six-component balance is used for measuring the drag force on the turbine (and on the disc, see Sec. II C). The device is provided with six Wheatstone bridges which are able to measure three components of force, in the axial, radial, and vertical directions, and three components of moments, in the rolling, pitching, and yawing directions with an accuracy of the balance is $\pm 0.23\%$ of the measured load. The turbine blades and nacelle are coated with a black paint for dimming the reflection of the laser beam. More information on the wind turbine design and the characteristics of the balance are provided in a similar investigation by Lignarolo *et al.* (2014a). The results of the thrust measurements are reported by Lignarolo *et al.* (2014b). The thrust coefficient was calculated with the following equation:

$$C_t = \frac{T}{0.5\rho A U_\infty^2}, \quad (1)$$

where T is the thrust force applied by the wind on the disc/turbine, ρ is the air density, and A is the rotor/disc area and the value was $C_t = 0.93$. For triggering the *leapfrogging* instability, an asymmetry of the blade pitch angle is introduced. The blades are installed to the nacelle hub

TABLE I. Experimental parameters (Lignarolo *et al.*, 2014b).

Parameters		WT	AD
Free-stream velocity	U_∞	4.7 m/s	4.7 m/s
Free-stream turbulence intensity	TI_∞	0.5%	0.5%
Rotational frequency	v	109.3 rad/s (17.4 Hz)	...
Reynolds (chord based) blade root, $r/R = 0.20$	Re_{cr}	32 000	...
Reynolds (chord based) blade tip, $r/R = 1$	Re_{ct}	96 000	...
Reynolds (diameter based)	Re_D	188 000	188 000
Thrust coefficient (balance measurements)	C_t	0.93	0.93
Tip speed ratio	λ	6.97	...

with a pitch-angle difference of 0.5° : this acts as a constant trigger for the wake instability, similar to the studies of Bolnot *et al.* (2014).

C. Design of an actuator disc model

Several solutions for reproducing a “physical” actuator disc can be found in the literature, as discussed in Section I. The main design drivers are porosity, structural stiffness, and wake-flow uniformity. The porosity is a measure of the permeable area of the disc and it is defined as the ratio between the open area and the total area of the disc. In Figure 1, the results of five experiments found in wind energy literature are compared, showing a consistent decreasing drag coefficient with increasing porosity. Structural stiffness is important in order to avoid oscillations at the free edge of the disc, which would strongly compromise the quality of the flow in the wake. In Section I, examples have been given about stiff structure obtained by modelling the actuator disc with perforated metal plates or by employing a mesh composed by wooden sticks. However, for the present study, the metal-mesh solution adopted by Aubrun *et al.* (2013) and Aubrun *et al.* (2007) was chosen. A 0.6 m diameter porous disc is manufactured by stacking three layers of fine metal mesh with uniform porosity $\xi = 60\%$ and spacing $\delta = 1$ mm with two additional larger meshes for structural stiffness ($\delta = 10$ mm and $\delta = 50$ mm, respectively) as shown in Figure 2. Mesh A has the double function of fine-tuning the drag coefficient and of flattening the underlying layers of fine mesh, whereas mesh B has the only function of supporting and stiffening the entire structure. A disc with total porosity $\xi = 32\%$ and drag coefficient $C_D = 0.93$ (equal to the turbine $C_t = 0.93$) is obtained. This is consistent with the results of previous experiments in Figure 1. The total thickness of the disc is 4 mm, which is 0.6% of the disc diameter. A uniform porosity disc has been adopted, disregarding the distribution of loads on the WT blades. The uniform disc of porosity $\xi = 32\%$ matches the thrust coefficient of the WT at tip-speed ratio $\lambda = 6.97$. Also, the disc is coated with a black paint for dimming the reflection of the laser beam. Section III B presents a comparison between two different methods for calculating the thrust coefficient. The disc structure was connected to the same nacelle of the turbine: in this way, both wakes show the same nacelle flow and all differences are only due to the presence or absence of the blades.

D. Experimental conditions

The measurements were performed in the wakes of the two models up to 2.2 diameters downstream, with multiple fields of view (FOV) in a horizontal plane at the hub height. The positions of the fields of view are represented in Figure 3, where each squared window

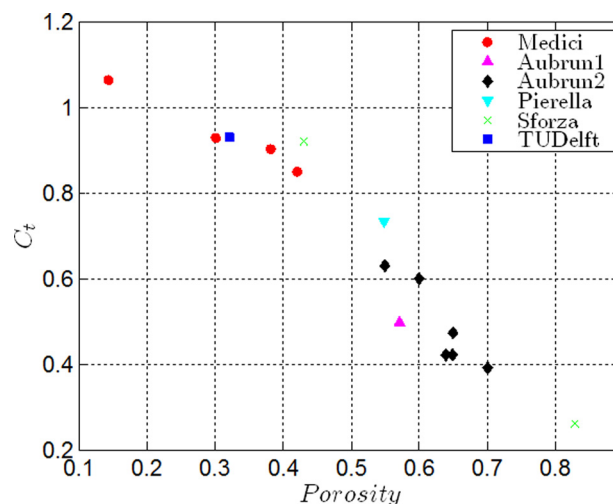


FIG. 1. Porous-disc drag coefficient as a function of porosity for several cases in literature.

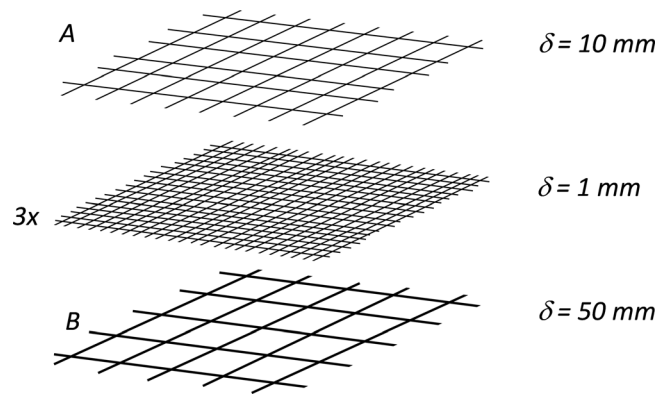


FIG. 2. Porous disc structure (not in scale).

represents an FOV in the horizontal plane. The darker shade between the windows shows the overlap between two adjacent FOV, which is 0.05 m in the axial and radial direction. The size of each field of view is $0.297 \times 0.227 \text{ m}^2$ (0.50×0.39 diameters). The measurement plane is parallel to the ground and perpendicular to the tower; therefore, the wake measurements do not exhibit any tower effect and the wake can be considered symmetric. For this reason, only one flow in half of the wake is captured. The distance between the turbine and the wind tunnel exit is approximately 1 rotor diameter. Table I summarises all relevant parameters about the experimental conditions. For each FOV, 200 unconditionally sampled three-component SPIV vector fields are averaged in order to obtain the mean velocity fields and second order turbulence statistics. Lignarolo *et al.* (2014a) have shown that such number of samples in very similar experimental conditions is sufficient for having a well-converged flow statistics. In four particular FOVs (near and far wake of the AD and near and far wake the WT, see Figure 22 in Sec. III F), a much larger number of samples have been taken (1000 for the AD and 5000 for the WT). The velocity fields in each FOV are combined with a simple stitching algorithm, selecting only one field in the overlapping region. No smoothing nor averaging is applied to the data.

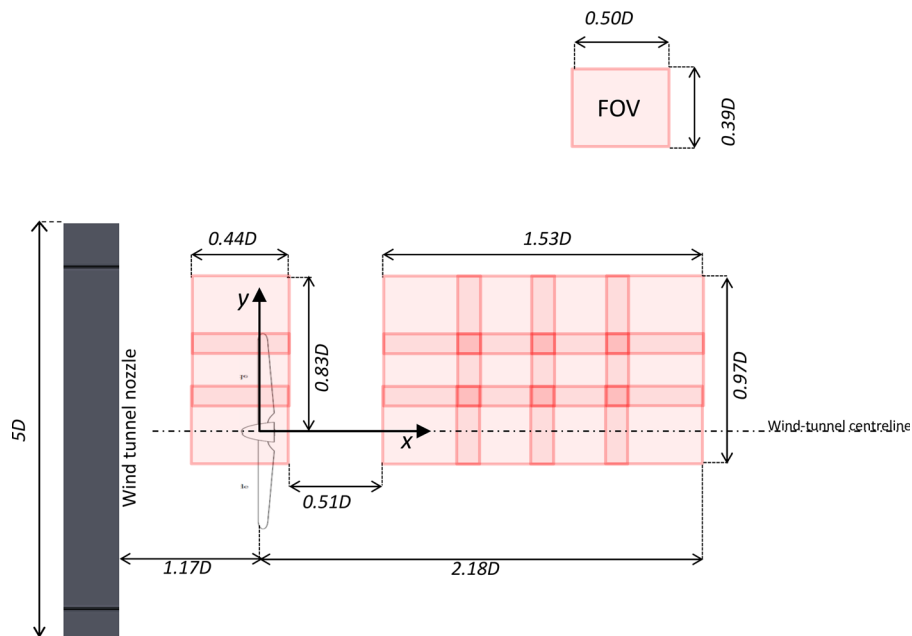


FIG. 3. Flow-field measurement configuration.

E. Stereoscopic particle image velocimetry

The three-component velocity fields in the rotor wake are obtained with SPIV experiments; the total vector field is obtained by stitching the results from different fields of view, as detailed in Figure 3. A traversing system, supporting the whole set up, enables to scan the flow field in the wake of the horizontal-axis wind-turbine wake, translating in 2D of about $1.2\text{ m} \times 0.9\text{ m}$. A Quantel Evergreen Nd:YAG laser system, with an average output of 200 mJ/pulse, provides the required illumination. The laser light is conveyed to form a 2 mm laser sheet of about 0.4 m width at the field of view. Images with a field of view of $0.297 \times 0.227\text{ m}^2$ (0.50×0.39 diameters) are acquired with two LaVision Imager Pro LX 16 Mpix ($4870 \times 3246\text{ px}^2$, 12 bits) with pixel pitch of $7.4\text{ }\mu\text{m/px}$. Two Nikon lenses of $f=180\text{ mm}$ and an aperture $f\#=2.8\text{--}4$ have been used. The obtained magnification factor is $M=0.10$. The focusing plane has been slightly offset with respect to the laser plane (defocusing), to obtain an image of the particle of about 2–3 px. Therefore, no bias error due to peak-locking is expected (Westerweel, 1997). Seeding was provided in the test section by a SAFEX smoke generator with SAFEX MIX, and able to produce liquid droplets of less than $1\text{ }\mu\text{m}$. Double-frame recordings have been acquired and processed with LaVision Davis 8.1.4; the final interrogation window size is $24 \times 24\text{ px}^2$ with 50% overlap, with a resolution of 1.46 mm and a vector spacing of 0.732 mm.

Table II summarises the main parameters of the stereo PIV setup.

F. Theory

The mean-flow kinetic-energy transport in the wake shear layer is evaluated in two selected locations, before and after the leapfrogging phenomenon. Results are compared in the wake of the WT and of the AD. The transport equation of the mean-flow kinetic-energy (2) is obtained as by Hamilton *et al.* (2012), with a Reynolds double decomposition of the flow where \bar{u}_i is the time average velocity in the i -direction and \bar{K}_E is the mean-flow average kinetic energy, p is the pressure, and $\overline{u'_i u'_j}$ are the Reynolds stresses. The third term of the right-hand-side of Eq. (2) represents the spatial gradient of the mean-flow kinetic-energy fluxes

$$\bar{u}_j \frac{\partial \bar{K}_E}{\partial x_j} = -\frac{1}{\rho} \frac{\partial \bar{p} \bar{u}_i}{\partial x_i} - \left(-\overline{u'_i u'_j} \right) \frac{\partial \bar{u}_i}{\partial x_j} - \frac{\partial}{\partial x_j} \left[\bar{u}_i \left(\overline{u'_i u'_j} \right) \right]. \quad (2)$$

When the equation is applied to a control volume including the wake shear layer but not encompassing the AD/WT, as shown by Lignarolo *et al.* (2015a) for $i=1$ and $j=2$, the term $\bar{\Phi} = -\bar{u}(\overline{u'v'})$ represents the flux in the radial direction of the streamwise mean-flow kinetic-energy. In other words, the term represents the entrainment of free-stream kinetic energy across the wake shear layer. It must be noted that a positive flux, meaning positive entrainment of kinetic energy toward the inner part of the wake, can happen only in case of a negative correlation between u' and v' ($\overline{u'v'} < 0$). This condition is satisfied in case of a turbulent bursts of slow speed fluid directed away from the wake centreline ($u' < 0$ and $v' > 0$) or in case of turbulent bursts of high speed fluid directed downward toward the inner part of the wake ($u' > 0$ and $v' < 0$).

TABLE II. System parameters of the SPIV setup (Lignarolo *et al.*, 2014b).

Parameters		SPIV setup	
Measurement field of view	FOV	$297 \times 227\text{ mm}^2$	$4870 \times 3246\text{ px}^2$
Interrogation window size	I_w	$1.46 \times 1.46\text{ mm}^2$	$24 \times 24\text{ px}^2$
Vector spacing (with 50% overlap)	S	0.732 mm	12 px
Digital resolution	DR		16.40 px/mm
Vectors	$N\#$		404×270

III. RESULTS

A. Global velocity field and indirect thrust calculation with momentum deficit

In Figures 4–6, the time-averaged wake normalised velocities fields $(u,v,w)/U_\infty$ are shown up to $x/D=2.2$ downstream the rotor/disc location. A mask has been applied to the areas encompassing the disc and the rotor. However, the thickness of this mask is not only representative of the physical thickness of the disc and the rotor themselves but also accounts of the regions affected by laser reflections and shadowing. As noted by Lignarolo *et al.* (2014a), in Figure 4 a localized increase of the wake shear layer thickness is visible starting from $x/D=1.5$ downstream the turbine wake and with maximum at $x/D=1.75$, corresponding to the leapfrogging region. For a tip-speed ratio $\lambda=6$, Lignarolo *et al.* (2014a) found the onset of the pairing instability at $x/D=1$ and showed that the phenomenon has a strong dependency on the tip-speed ratio and on the vibration introduced by the mounting conditions (with higher tip-speed ratios, or more structural vibration, leading to earlier instability). Figure 5 shows a localised region of strong positive radial velocity in both the AD and the WT wake due to the sudden wake expansion. The contours show that this phenomenon is mainly concentrated at the tip location. The rest of the AD wake (Figure 5, top) is characterised by a generally positive and close to zero radial velocity. On the contrary, the WT wake (Figure 5, bottom) shows also a large region of negative radial velocity at the root region. This could be ascribed to an interaction between the wake rotational motion and the tower's wake (not present in the measurements) that causes a wake asymmetry. The same phenomenon is also visible by Schümann *et al.* (2013) and by Medici (2005): although the latter reported negative values of radial velocity only after 2 diameters, the form recorded negative values also in the very near wake and a visible wake asymmetry due to the tower effect. A second region of negative radial velocity appears at about $x/D=1.5$ in Figure 5 (bottom) after the tip-vortex instability location, due to the entrainment of the external flow. Figure 6 contains the contours of normalised azimuthal velocity \bar{w}/U_∞ , which as expected is nearly null in the AD wake. In the WT wake, the out-of-plane contribution is instead counter rotating with respect to turbine rotation (negative for $y/D > 0$ and positive for $y/D < 0$). An interesting feature of Figure 6 (top) is the region of positive \bar{w}/U_∞ at the upper edge of the WT wake, which then develops into a region of negative

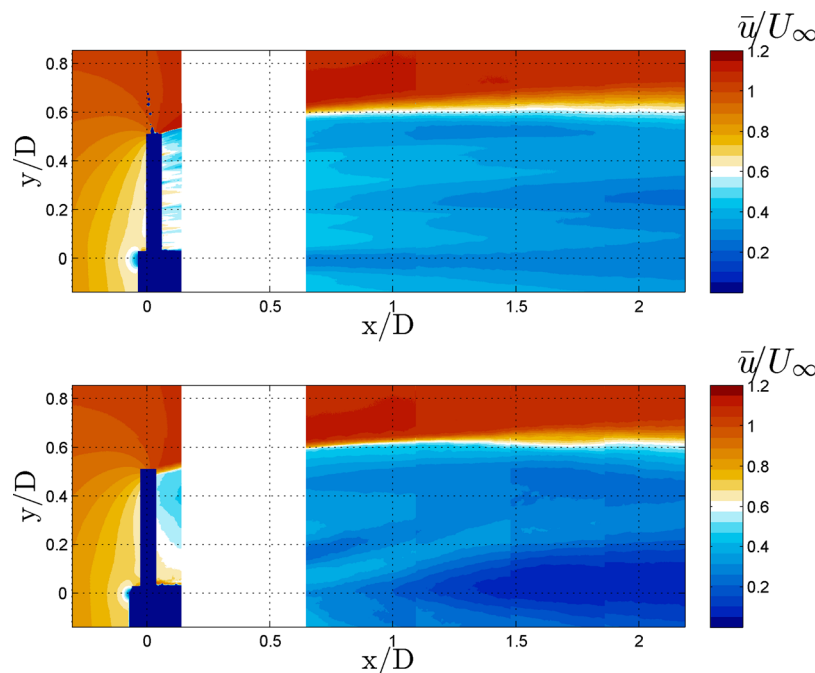


FIG. 4. Axial (x -direction) velocity field in the wake of the AD (top) and of the WT (bottom).

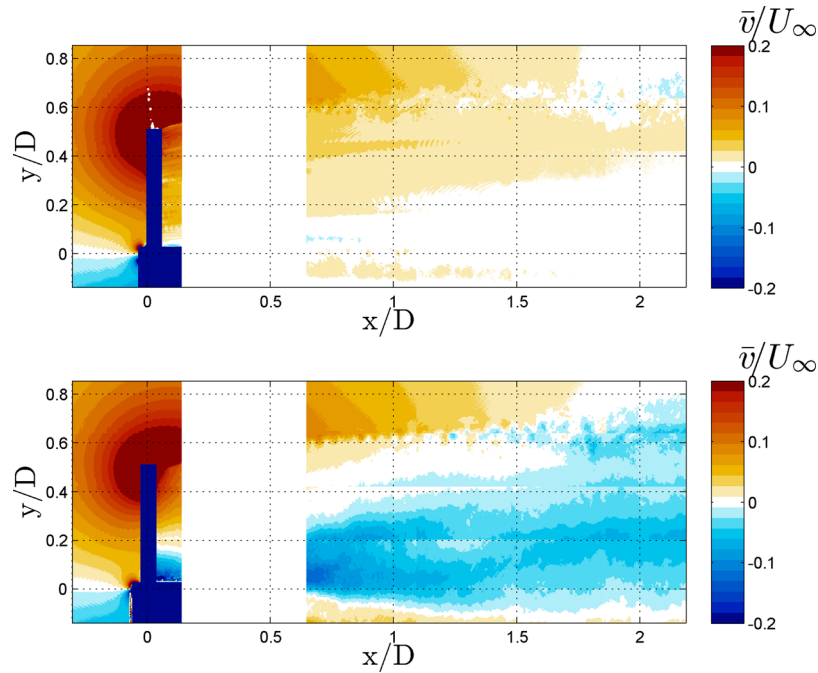


FIG. 5. Radial (y -direction) velocity field in the wake of the AD (top) and of the WT (bottom).

\bar{w}/U_∞ with absolute value larger than the surrounding field from $x/D = 1.5$. This is consistent with the findings of Lignarolo *et al.* (2014a), who showed a clear change of sign in the azimuthal velocity direction close to the vortex core after the leapfrogging location. Figures 7–9 show the normalised velocity profiles \bar{u}/U_∞ , \bar{v}/U_∞ and \bar{w}/U_∞ at five different downstream locations. The first location is very close to the rotor/disc (0.1D); the second at an undisturbed location before the instability (0.7D); the third location is right at the beginning of the leapfrogging

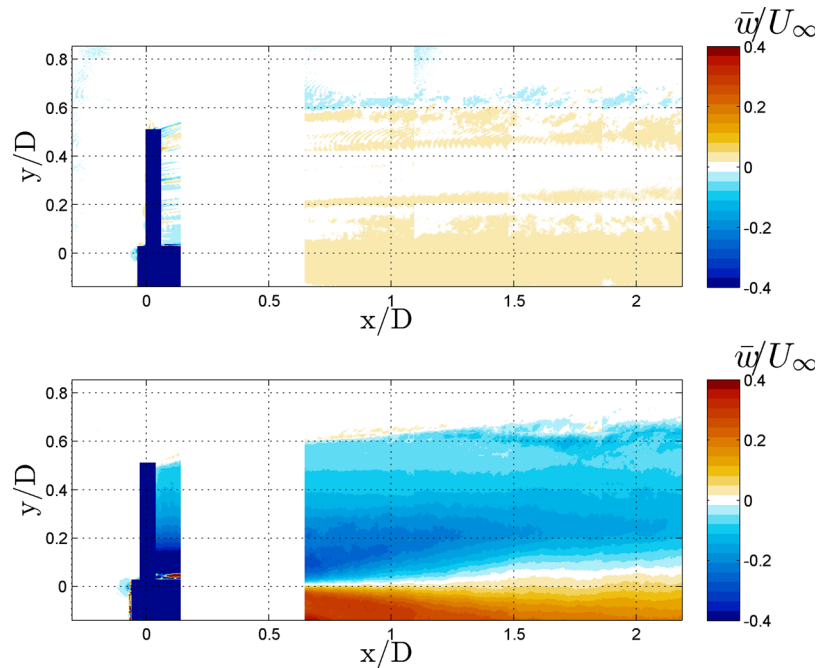


FIG. 6. Azimuthal (z -direction) velocity field in the wake of the AD (top) and of the WT (bottom).

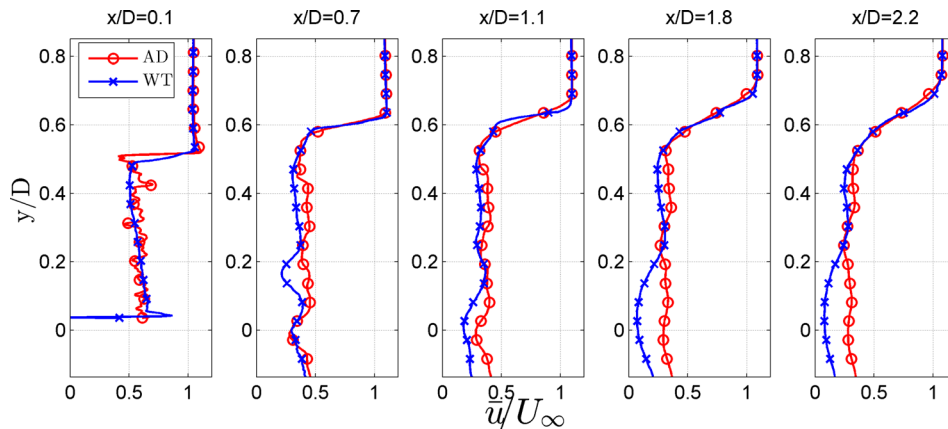


FIG. 7. Axial (x -direction) velocity profiles at five different locations in the wake of the AD and of the WT.

region ($1.1D$); the fourth is in the middle of the leapfrogging region ($1.8D$); and the last location is at the end of the measurement area ($2.2D$). The plots confirm the analysis of Figures 4 and 5. At $x/D = 0.1$, the mean axial velocity profile in the AD wake shows dishomogeneity compared to the WT wake velocity profile with $\Delta\bar{u}/U_\infty = \pm 0.1$. Lignarolo *et al.* (2014b) explained that this is due to the different process of wake generation. The metal mesh of the AD does not extract mechanical energy from the flow as the WT, but it dissipates the kinetic energy of the incoming wind into turbulence, which quickly decays (Batchelor and Townsend, 1947; 1948a; and 1948b). At $x/D = 0.8$ and $x/D = 1.1$ upfront the leapfrogging region, the presence of the tip vortices at the border of the WT wake induces a sharp velocity gradient. On the contrary, the AD wake shows a smoother velocity variation. After the instability location, the WT and the AD wakes become more similar: as a matter of fact, the tip vortices break down and the velocity gradient in the shear layer is less strong. The largest differences between the two velocity profiles are in the region between $y/D = -0.1$ and $y/D = 0.2$, with $\Delta\bar{u}/U_\infty = \pm 0.25$. The expansion of the two wakes is calculated, with the wake border being the locus of the points where the velocity is 99% of U_∞ . Matching diameter and thrust coefficient of the two models should ensure the same wake expansion Lignarolo *et al.* (2014b). As a matter of fact, Figure 10 demonstrates that the wake expansion is very similar in the AD and WT wakes, with the relative difference, calculated as $(\text{expansion}_{AD} - \text{expansion}_{WT})/\text{expansion}_{WT}$, everywhere lower than 4%.

A second method for calculating the thrust coefficient is by indirect calculation from the velocity field, by integrating the momentum deficit in the wake. This is compared to the value

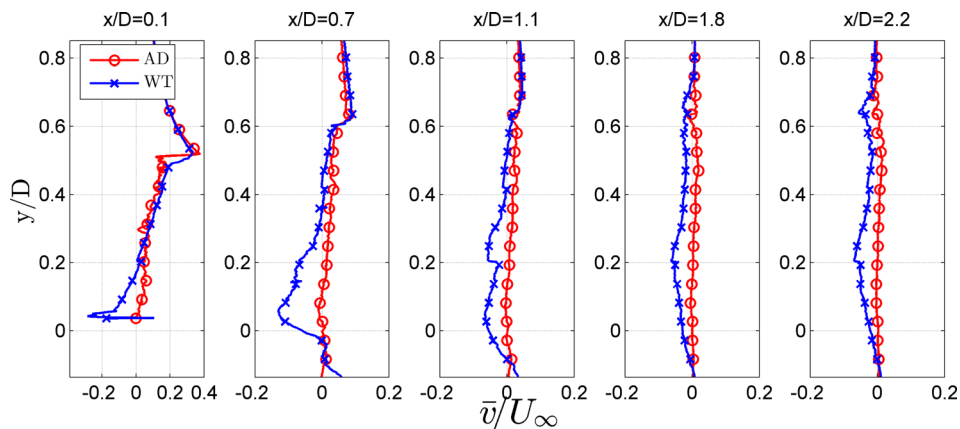


FIG. 8. Radial (y -direction) velocity profiles at five different locations in the wake of the AD and of the WT.

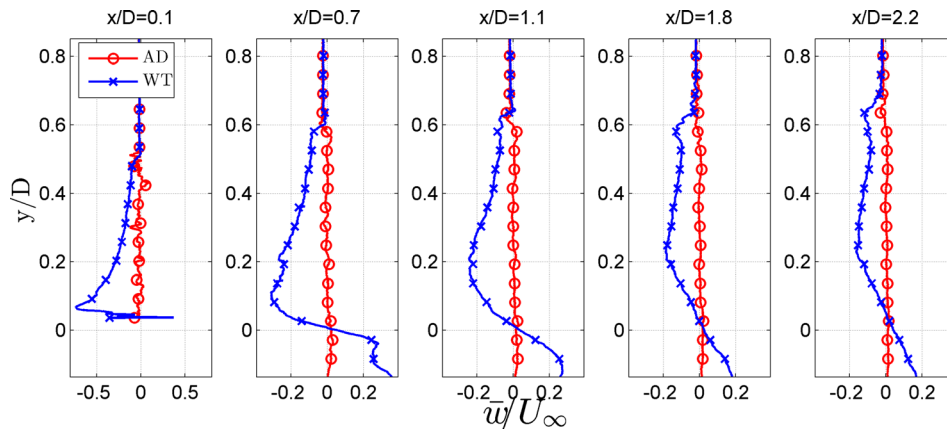


FIG. 9. Azimuthal (z -direction) velocity profiles at five different locations in the wake of the AD and of the WT.

obtained with direct measurement via the 6-component balance. In this case, the thrust coefficient has been calculated using Equation (3) from [Burton *et al.* \(2001\)](#), with the strong assumption of Bernoulli equation being applicable separately to the upstream and downstream sections of the stream-tube

$$C_t = 4a(1 - a), \quad (3)$$

where a is the induction factor (see [Lignarolo *et al.* \(2014b\)](#) equations) and it is equal to $a = 0.388$ for the WT and $a = 0.376$ for the AD. The thrust coefficient is $C_t = 0.949$ for the WT and $C_t = 0.938$ for the AD, respectively, 2.0% and 0.86% higher than the balance measurement.

B. Static pressure and indirect thrust calculation with pressure jump

The static pressure field at the rotor/disc location can be calculated directly from the SPIV data. The derivation of the pressure from SPIV data has been extensively addressed in many fields of research, as by [Liu and Katz \(2006\)](#), [Raffel *et al.* \(1998\)](#), [Ragni *et al.* \(2011\)](#), and [van Oudheusden \(2013\)](#). Applications in phase-locked environments for propeller and wind-turbines have allowed reconstructing the 3D periodic pressure fields and subsequently non-intrusively obtaining loads on the rotor blade by [Ragni *et al.* \(2011\)](#). [Lignarolo *et al.* \(2014a\)](#) have used this method for calculating the phase-locked average pressure field in the wake of the same

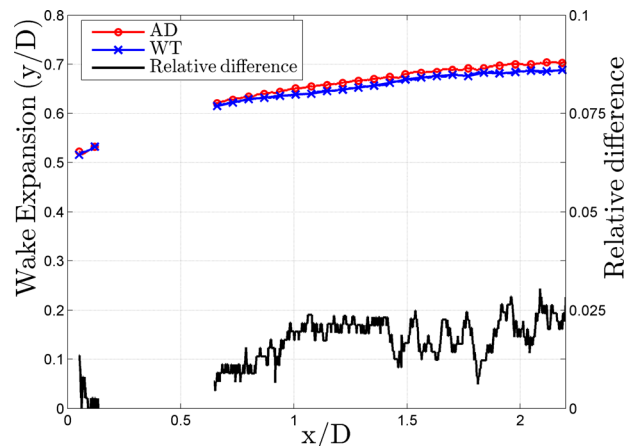


FIG. 10. AD and WT wake expansion and relative difference. The curves represent the loci of the points where the axial velocity is 99% of the free stream value.

rotor model used in the present work. The method allows reconstruction of the pressure field from its own gradient obtained from the Navier-Stokes momentum equation

$$\frac{\partial p}{\partial x_i} = -\rho \left(\frac{\partial u_i}{\partial t} + u_j \frac{\partial u_i}{\partial x_j} \right) + \mu \frac{\partial^2 u_i}{\partial x_i \partial x_j}, \quad (4)$$

where ρ and μ are, respectively, the flow density and the dynamic viscosity assumed constant. However, in the present analysis, due to the high Reynolds number, the viscous terms have been neglected compared to the inertial contribution. The time derivative of the velocity is null, because data are time averaged (axisymmetric wake). Also, gradients along the z -direction have been neglected, because much smaller than the other quantities. The equation is as such reduced to its two-dimensional steady-state version. The pressure integration is performed by rewriting the Poisson's equation into a 2D Poisson scheme. The pressure integrator used in the present manuscript is based on the version in use by Ragni *et al.* (2011). The algorithm solves the Poisson's equation (5), where the pressure gradient is calculated as in (4), inverting a linear system of equations obtained through a second order finite difference scheme in 2D. Dirichlet (Bernoulli pressure) and Neumann boundary conditions are applied to solve the Poisson's equation

$$\nabla^2 p = \frac{\partial}{\partial x_i} \frac{\partial p}{\partial x_i}. \quad (5)$$

The pressure integration is performed in an area spanning from $0.3D$ upstream until $0.15D$ downstream the rotor/disc location on the axial direction and from the turbine axis up to $0.85D$ distance along the radial direction. The results are shown in Figure 11, where the c_p is calculated as

$$c_p = \frac{2p}{\rho U_\infty^2}. \quad (6)$$

For allowing a smooth calculation of the velocity gradients, the velocity fields have been interpolated in proximity of the rotor/disc using a least squares approach, where data are compromised due to the presence of shadowing and reflection from the model itself (see masks applied in velocity, vorticity, and turbulence fields throughout the whole article). This also explains the much thinner mask applied to the field in Figure 11 compared to the one used in Figures 4–6. Figure 11 (left) compares the streamwise development of pressure at 4 radial locations in the AD and WT wake. A strong pressure jump is evident at $x/D=0$ consistently with the presence of the model. Results from the AD and the WT agree within a difference lower than 8% everywhere, with larger differences up to 20% in the tip and root location at $y/D=0.07$ and $y/D=0.29$. Figure 12 (left) depicts the pressure profiles along the upwind and downwind surfaces

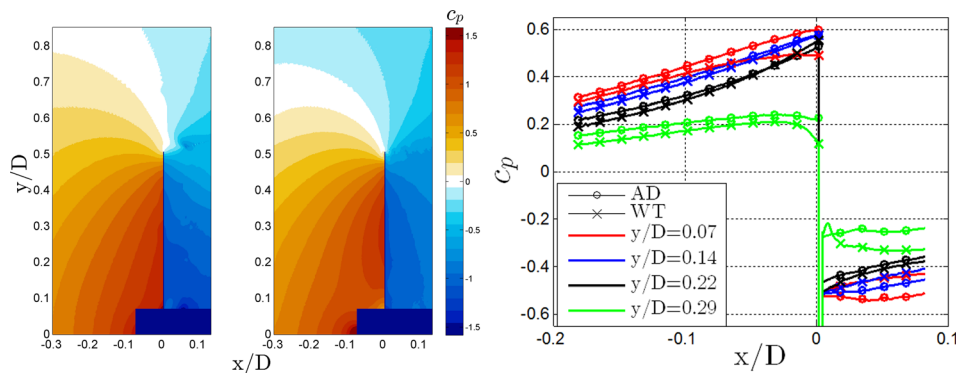


FIG. 11. Pressure distribution at the disc (left) and rotor (center) location. On the right: streamwise development of pressure at different radial locations across the AD and WT.

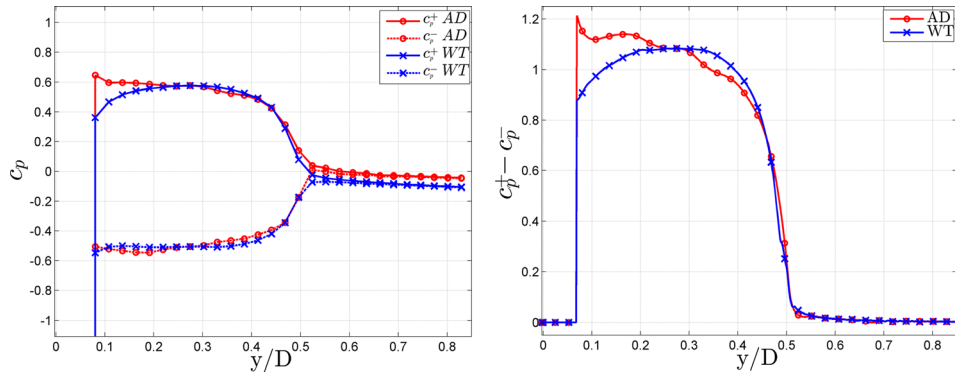


FIG. 12. Left: pressure distribution along upwind and downwind surface of the AD and the WT. Right: pressure jump across the AD and WT along the radial direction.

(respectively, c_p^+ and c_p^-) of the disc and rotor, showing the strong root effect from $y/D = 0.08$ and $y/D = 0.2$, visible in the c_p^+ curves. The pressure jump across the disc/rotor is shown in Figure 12 (right). This value can be integrated on the disc/rotor surface as shown in (7) for calculating the thrust coefficient, yielding a thrust coefficient of $C_t = 0.934$ for the AD and $C_t = 0.927$ for the WT, respectively, 0.43% higher and 0.32% lower than the balance measurement

$$C_t = \frac{4\pi}{A} \int_{R_{root}}^{R_{tip}} (c_p^+ - c_p^-) r dr. \quad (7)$$

Table III summarises the AD and WT thrust coefficients calculated with the three methods (with the six-component balance, from velocity field, from pressure field) and shows the relative difference between them.

C. Stagnation enthalpy

With no net shaft work and heat transfer, the stagnation enthalpy is constant along each streamline for a frictionless non-conducting fluid in motion with a steady pressure distribution (Batchelor, 2000). A wind turbine extracts power from the flow in the form of shaft work; therefore in this case, the flow experiences a drop of enthalpy. For this reason, the variation of stagnation enthalpy is the best indicator of the amount of power \dot{W} extracted from the flow by the rotor, which can be calculated as $\dot{W} = -\dot{m}\Delta h$, where \dot{m} is the mass flow rate across the rotor area A , and Δh is the difference between the stagnation enthalpy in the wake region and the one of the free-stream flow H_∞ . The variation of stagnation enthalpy per unit mass is calculated as

$$\Delta h = \Delta e + \frac{\Delta p}{\rho} + \Delta q + \Delta \Psi, \quad (8)$$

TABLE III. Values of AD and WT thrust coefficient C_t , obtained with direct balance measurements and by indirect calculations (from velocity and pressure).

Method	AD	WT	Relative difference (%)
Direct (balance)	0.930	0.930	0
From velocity field	0.938	0.949	-1.17
From pressure field	0.934	0.927	0.75

where Δe is the variation of internal energy of the flow per unit mass, Δp is the static pressure variation estimated from the SPIV velocity field as in Sec. III B, $\Delta q = 0.5(\Delta u^2 + \Delta v^2 + \Delta w^2)$ is the variation of the flow kinetic energy per unit mass and $\Delta \Psi$ represents the variation of body forces. The latter one can be neglected in absence of substantial variation of potential energy as in this case. Also, in the absence of heat transfer, the flow temperature across the wind turbine can be considered constant and the variation of internal energy null, with an acceptable approximation. Therefore, the power extracted by the wind turbine can be calculated as

$$\dot{W}_{WT} = -\dot{m} \left(\frac{\Delta p}{\rho} + \Delta q \right)_{WT}. \quad (9)$$

The flow across the disc does not experience a power extraction through shaft work nor external heat transfer ($\Delta h = 0$), but rather a degradation of the inflow kinetic and pressure energy into heat through turbulence dissipation. The pressure energy and the kinetic energy variations are therefore balanced by a variation of internal energy, which is calculated as

$$\dot{E}_{AD} = -\dot{m} \left(\frac{\Delta p}{\rho} + \Delta q \right)_{AD}, \quad (10)$$

with $\Delta h = 0$. The contours in Figure 13 (left) show the value of $-\Delta e/H_\infty$ in the AD wake flow. The contours in Figure 13 (centre) show the value of $\Delta h/H_\infty$ in the WT wake flow. Figure 13 (right) shows the profiles of $-\Delta e/H_\infty$ and $\Delta h/H_\infty$ at $x/D = 0.1$. It is evident how the internal energy variation in the AD wake corresponds very well to the stagnation enthalpy variation in the WT wake. The normalised power dissipated by the AD and the one extracted by the WT are calculated, respectively, in Eqs. (11) and (12)

$$C_{p,AD} = \frac{4\pi}{U_\infty^3 A} \int_{R_{root}}^{R_{tip}} \bar{u}(r, x=0) \Delta e(r) dr, \quad (11)$$

$$C_{p,WT} = \frac{4\pi}{U_\infty^3 A} \int_{R_{root}}^{R_{tip}} \bar{u}(r, x=0) \Delta h(r) dr. \quad (12)$$

The calculation leads to a normalised power $C_{p,AD} = 0.593$ for the disc and $C_{p,WT} = 0.578$ for the wind turbine. The relative difference between them is equal to 2.53%, of the same order of magnitude of the wake expansion relative difference. Knowing C_t from the balance

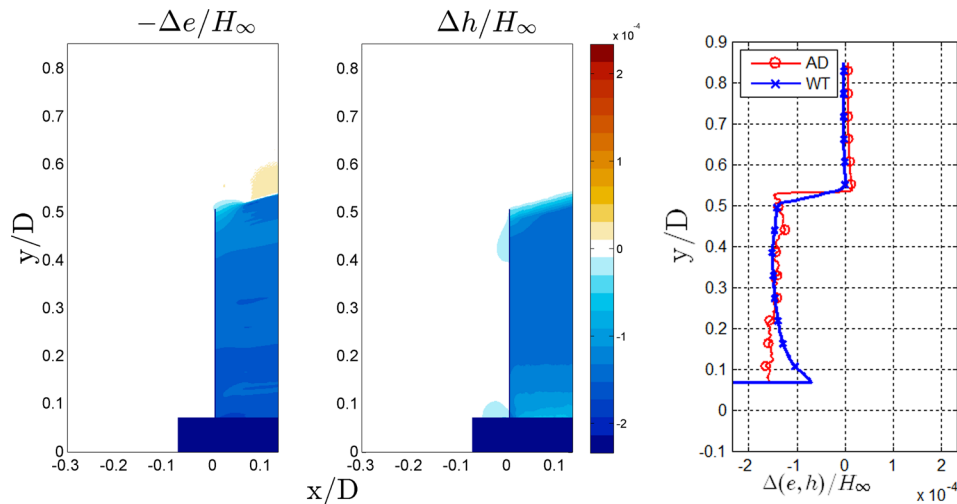


FIG. 13. Stagnation enthalpy distribution at the disc (left) and rotor (centre) location. On the right: radial profile of stagnation enthalpy at $x/D = 0.1$ for the AD and the WT.

measurements, the expected induction factor a is calculated with (3) and used for calculating the expected power coefficient with Equation (15) of Burton *et al.* (2001)

$$C_p = 4a(1 - a)^2. \quad (13)$$

Table IV summarises the AD and WT power coefficients calculated with the two methods (expected from balance measurements and from enthalpy field) and shows the relative difference between them.

For the actuator disc, the C_p calculated with this method is very close to the Betz limit. As a matter of fact, the disc was designed for having an induction factor close to the optimum value. However, the device does not involve an actual extraction of energy from the flow, but the kinetic energy of the incoming flow is converted into turbulence and eventually heat. In fact, a physical emulation of the actuator disc (the latter is only a theoretical model) does not obey the Betz theory. The C_p of the wind turbine is also very close to the Betz limit because also the WT was designed for quasi-optimal operation. However, the C_p is not calculated with the power available at the shaft, but with the energy extracted from the flow. For this reason, the efficiency is quite high, but a considerable part of it is still wasted in heat for viscous effects and in friction inside the nacelle.

D. Vorticity field

Figure 14 shows the value of the out-of-plane time-average vorticity, calculated as

$$\bar{\omega}_z = \frac{\partial \bar{v}}{\partial x} - \frac{\partial \bar{u}}{\partial y}. \quad (14)$$

The derivatives are estimated with a second-order finite-difference scheme. Results in Figure 14 (top) show that the AD vorticity is organised as a very concentrated sheet of negative vorticity close to the disc at the tip region which diffuses very quickly. As a matter of fact, at $x/D = 0.6$ the vortex sheet has already diffused in a broader region. Figure 14 (bottom) shows that, on the contrary, the WT wake shows a less concentrated vortex sheet that nonetheless diffuses more slowly, preserving its strength for longer distance.

As also shown by Lignarolo *et al.* (2014a), the WT vortex sheet bifurcates at the location where the vortex leapfrogging occurs, after which it eventually breaks down and diffuses quite rapidly. The vorticity in the AD and WT wake are comparable only after the tip-vortex instability. In the very near wake, the flow vorticity is higher in the AD wake shear layer; in the second and third locations, while the tip-vortices are still stable, the vorticity in the WT shear-layer exceeds the one in the AD wake, while after the tip-vortex breakdown the values of vorticity are comparable in the two wakes. The inner part of the wake also shows some regions of positive vorticity. In the AD wake, these regions constitute the smaller wakes of the wires of mesh B (see Figure 2). In the WT wake, regions of positive vorticity are due to the presence of the root vortex. Figure 15 depicts the development in the axial direction of the maximum value of vorticity in the AD and WT vortex sheet. The AD initial value of vorticity is three times as large as the WT one and decreases exponentially until $\omega_{z,max}D/U_\infty < 10$ within 2D. For the development of the WT vorticity, three regions can be identified. The first region, in the very near wake before $x/D = 0.5$, is characterised by an increase of the maximum vorticity from of

TABLE IV. Values of AD and WT power coefficient C_p as expected from direct balance measurements and by indirect calculation.

Method	AD	WT	Relative difference (%)
Expected (from balance measurements)	0.588	0.588	0
From enthalpy field	0.593	0.578	2.53

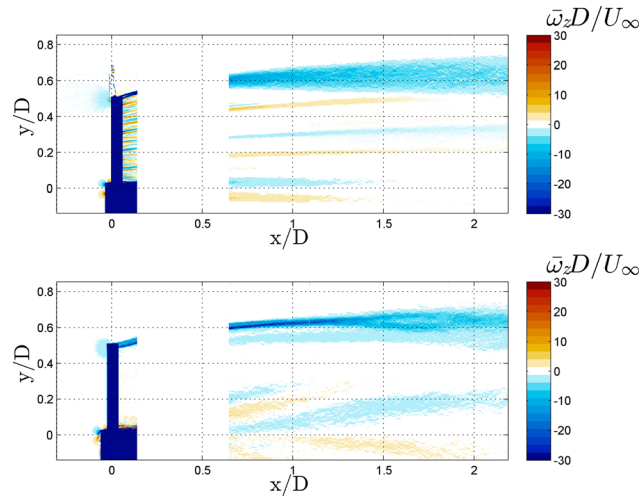


FIG. 14. Out-of-plane vorticity field in the wake of the AD (top) and of the WT (bottom).

about 20%. Since a considerable portion of the flow field is not available in this region, results from the previous experimental campaign (Lignarolo *et al.*, 2014a) for a similar configuration have been included in the graph of Figure 15. It is evident how also in this case the near wake vorticity is subjected to an increase which might be due to the tip-vortex stretching, caused by the fast wake expansion. As a matter of fact, in the region between $x/D=0$ and $x/D=0.5$ 50% of the wake expansion takes place, as shown in Figure 10. The second region is characterised by a linear decrease of the peak value of vorticity until the location of the tip-vortex breakdown at $x/D=1.5$. From this location, the third region starts, where the peak vorticity decreases at a slower rate, comparable to the one of the AD wake.

E. Wake turbulence

In Figures 16–18, the three components of the time-average wake turbulence intensity is shown until 2.2D downstream: these figures show a general perspective on the whole wake

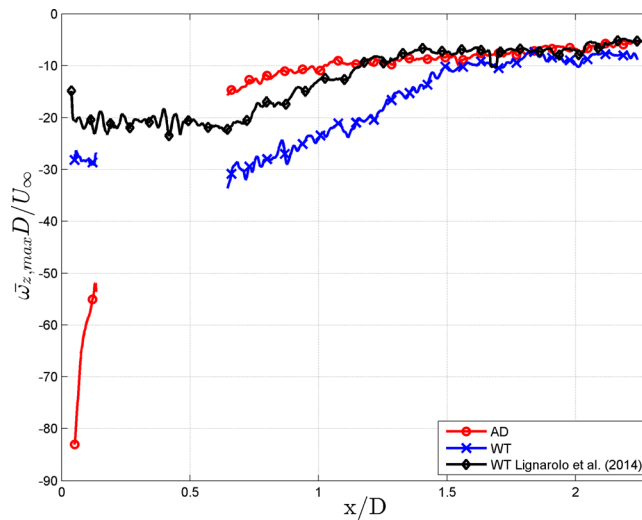


FIG. 15. Streamwise evolution of the maximum normalized vorticity in the vortex sheet at the edge of the wake. The three curves depicts, respectively, the values in the AD and WT turbine wake from the present experiments and in the WT wake from the experiments of Lignarolo *et al.* (2014a).

turbulence field. In Figures 19–21, the same quantities, shown as profiles at selected locations, allow a more precise reading of the values of TI . The WT and AD wake turbulence profiles exhibit more evident differences, compared to the velocity profiles in Figures 4–6. The turbulence intensity in the three directions is calculated as in the following equation:

$$TI_{x_i} = \frac{u_{i,RMS}}{U_\infty}, \quad (15)$$

where $u_{i,RMS}$ is equal to $\sqrt{u'u'}$, $\sqrt{v'v'}$, and $\sqrt{w'w'}$ for $i=1,2,3$, respectively. In this regard, it is very important to stress that the fluctuating terms of velocity u' , v' , and w' include any deviation from the mean value of velocity, either if this is caused by a turbulent fluctuation or by a coherent vortex. At a first general observation, both wakes show evident anisotropic turbulent fluctuations, demonstrated by the visible differences among the turbulence values in the three directions TI_x , TI_y , and TI_z . Both the AD and the WT profiles show a strong peak in turbulence intensity in correspondence of the wake shear layer. The analysis of the profiles of turbulence in each location (Figures 19–21) will help highlight the sensible differences in the two wakes. In the first location in Figures 19–21, the WT wake exhibits a peak of radial fluctuations intensity TI_y which is 33% larger than the peak of fluctuations in the axial direction TI_x . Coherently with previous literature studies from (Cotroni *et al.*, 2000), it has been found out that the radial fluctuations are the predominant ones. The out-of-plane fluctuations show a more uniform distribution in space, with a value which is roughly 50% of the TI_x peak. In the second location, the persistence of strong tip vortices keeps the peak of fluctuations in the x - and y -directions equal to their initial values. In the fourth and fifth locations, after the tip-vortex breakdown, the fluctuations in the radial direction collapse and the wake turbulence assumes rather isotropic characteristics, with similar values in TI_x , TI_y , and TI_z . In the out-of-plane direction, the fluctuation intensity keeps on increasing in the shear layer region from the first to the fifth locations. In the shear layer of the AD wake, the peak of turbulence intensity remains constant from the second location to the fifth location, with a value of the out-of-plane fluctuations always two times larger than the one in the x - and y -directions. The largest differences between WT and

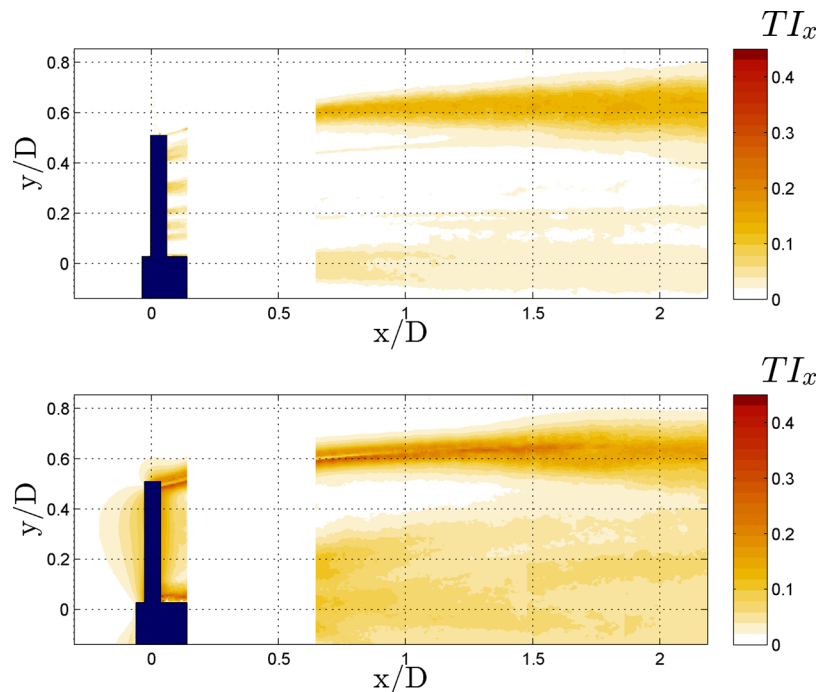


FIG. 16. Turbulence intensity in the axial (x -direction) direction in the wake of the AD (top) and of the WT (bottom).

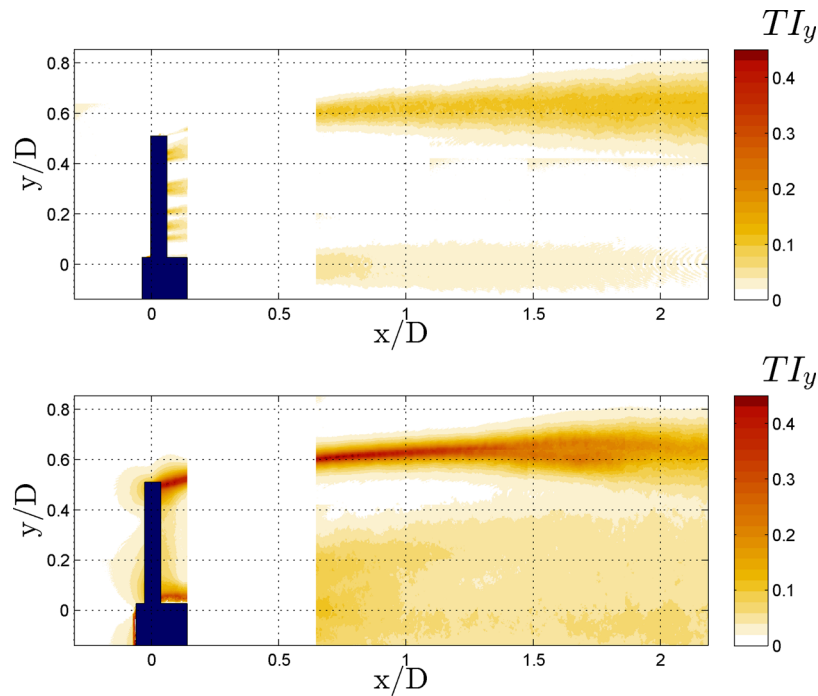


FIG. 17. Turbulence intensity in the radial (y -direction) direction in the wake of the AD (top) and of the WT (bottom).

AD wake turbulence appear within $1.8D$ from the model, where the peak of radial fluctuations in the WT wake is two to four times larger than the one in the AD wake. This behaviour is attributed to the convected tip-vortex in the WT wake. As a matter of fact, in the time-averaging process the tip vortex is considered as a turbulent fluctuation in the stream-wise and

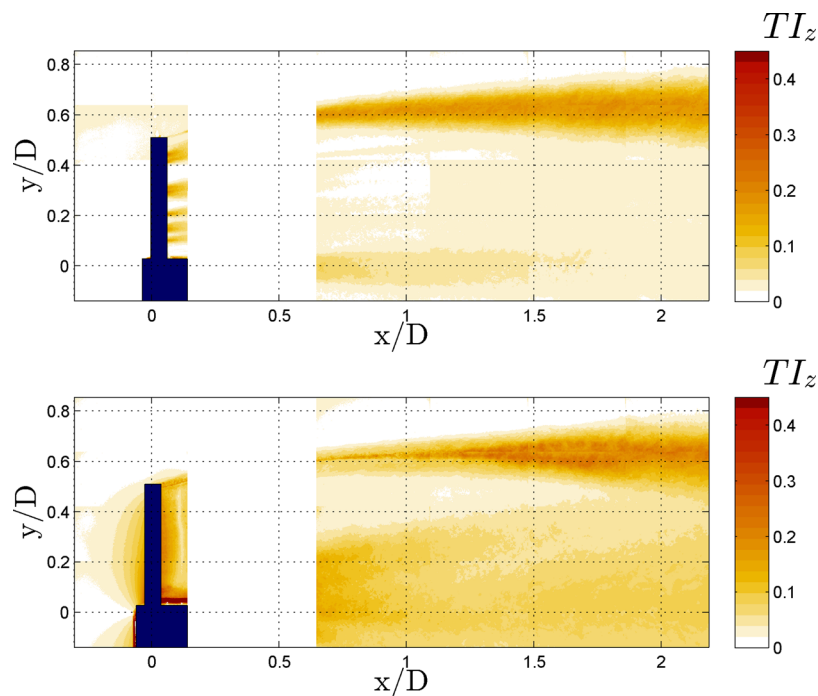


FIG. 18. Turbulence intensity in the out-of-plane (z -direction) direction in the wake of the AD (top) and of the WT (bottom).

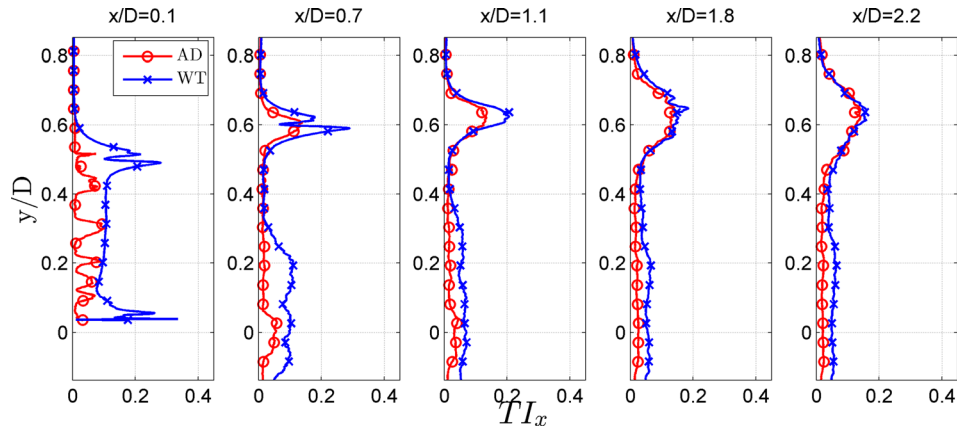


FIG. 19. Profiles of turbulence intensity in the axial direction (x -direction) at five different locations in the wake of the AD and of the WT.

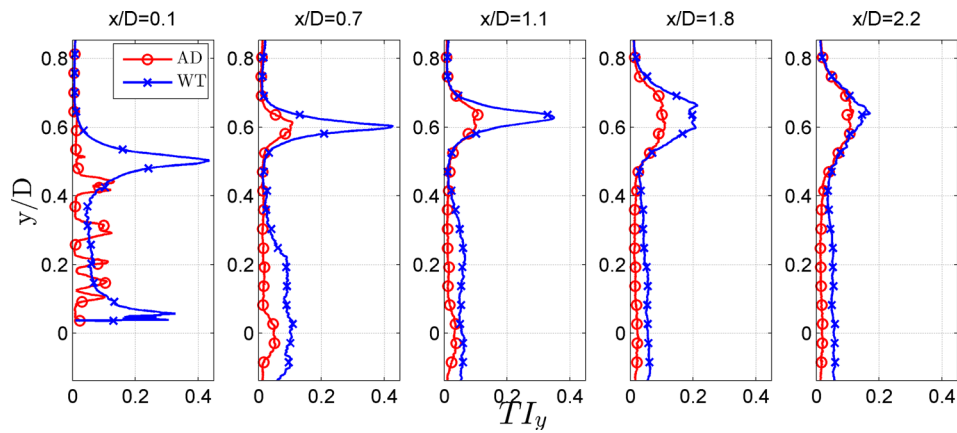


FIG. 20. Profiles of turbulence intensity in the radial direction (y -direction) at five different locations in the wake of the AD and of the WT.

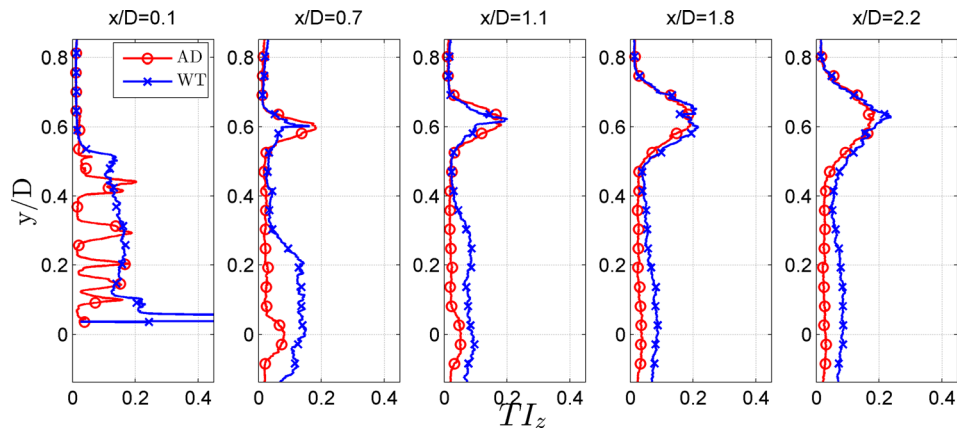


FIG. 21. Profiles of turbulence intensity in the out-of-plane direction (z -direction) at five different locations in the wake of the AD and of the WT.

radial directions (Lignarolo *et al.*, 2015a), which dissipates and diffuses after the instability and is not present in the AD wake. In the inner region of the wake, the presence of the WT blades turbulence is prominent. As a matter of fact, the WT wake is characterised by a turbulence intensity which is always higher than the AD one. The fine metal mesh in the AD generates turbulence characterised by smaller-scale structures that decay very quickly (Batchelor and Townsend, 1947; 1948a; and 1948b) and almost completely dissipate within one rotor radius, while the blade root generates vortex structures, which are more self-sustaining. Differences between WT and AD wake turbulence vanish downstream, after $x/D = 1.8$ (Lignarolo *et al.*, 2014b).

F. Wake mixing

Although the turbulence intensity could intuitively be associated with the flow mixing, it has been demonstrated that the Reynolds shear stresses uv , uw , and vw are responsible of the flow kinetic energy transport (Antonia *et al.*, 1986; Cal *et al.*, 2010; Cantwell and Coles, 1983; Escudé and Liné, 2003; Hussain, 1983; and Reynolds and Hussain, 1972) and that as such they must be taken into consideration for evaluating the turbulent mixing in a particular region of the flow. For this reason, the last term of Equation (2), which represents the spatial gradients of the flux of mean-flow kinetic energy, has been evaluated in the x - y plane as $\bar{\Phi} = -\bar{u}(\bar{u}'v')$ (streamwise mean-flow kinetic energy flux in the radial direction). As explained in Sec. II F, this term represents the entrainment of kinetic energy in the inner part of the wake. The schematic impression in Figure 22 shows the regions where the flux $\bar{\Phi}$ has been calculated, indicated by the green squares. The locations are in the near wake and in the transition wake, respectively, centred at $x/D = 0.95$ and $x/D = 1.83$. The first location is before the tip-vortex instability and the second is right after the beginning of the instability. In these locations, a large number of samples has been used for obtaining a good convergence of the Reynolds stresses $u'v'$ (1000 for the AD and 5000 for the WT). Figure 23 shows the radial profiles of the mean-flow kinetic energy fluxes towards the inner part of the wake as described in Sec. II F. The AD wake shear layer is characterised by a solely positive flux of mean-flow kinetic energy, whereas in the WT wake shear layer the more coherent flow fluctuations give rise to both positive and negative fluxes. In contrast with what expected after observing the strong peak of fluctuations intensity in Figures 19–21, where the WT exhibits a TI peak two to four times larger than the AD one, the WT wake shear layer does not show the same peak in mean-flow kinetic energy entrainment in the near wake region ($0 < x/D < 1.8$). On the contrary, the value of the entrainment in the two wakes is comparable, with the AD one involving a larger portion of the flow. In the WT wake both random fluctuations and periodic vortices are accounted for as turbulence, as mentioned in Sec. III E. Lignarolo *et al.* (2015a) have shown that the periodic vortical fluctuations do not lead to a net positive transport of mean-flow kinetic-energy (and therefore entrainment of energy in the WT wake). The entrainment in the AD wake shear layer is relatively stable, preserving the same intensity from the very near wake until the end of the measured field. On the contrary, the WT wake shear is characterised by pronounced variations of mean-flow kinetic energy flux. In particular in the transition wake, the magnitude of the entrainment collapses to a strong negative value within a distance smaller than $0.2D$ and reaches again positive values after $0.2D$. This behaviour was also observed by Lignarolo *et al.* (2014a) in the analysis of the Reynolds shear stresses. The sudden collapse to negative values is caused by the tip-vortex pairs changing orientation during the leapfrogging process, passing from a negative to a positive $u'v'$ (see Hussain, 1983). This latter topic is subject of current investigation. The subsequent low positive value of entrainment is caused by the vortex breakdown, which leads to the disappearance of the strong coherent vortical fluctuations and gives start to a new mixing process only dominated by random turbulent fluctuations. At $x/D = 2.04$, the flux intensity is roughly just 50% of the one in the AD wake, despite the WT TI is equal or slightly larger than the AD one as seen in Figures 19–21. This is the sign that turbulence intensity alone is not enough for analysing the mixing phenomenon.

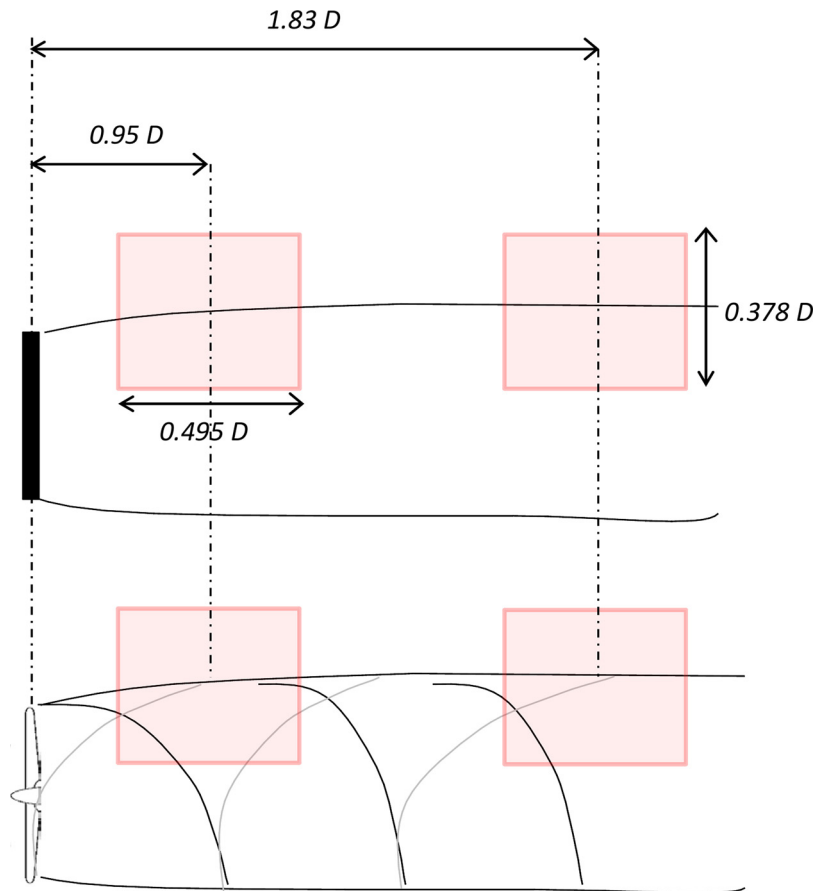


FIG. 22. Schematic impression of the measurement locations of the mean flow kinetic energy transport. The green areas represent the FOV (AD in the top image and WT in the lower image). Distances and dimensions are indicated by the blue lines.

IV. CONCLUSIONS

The stereo particle image velocimetry technique has been adopted for studying the turbulent velocity field in the wake of two-bladed wind-turbine model and of a porous disc. The analysis has shown that the two models produce remarkably similar wake expansion and energy extraction, within 4% difference for both quantities, by matching the diameter and thrust coefficient. Larger differences (locally up to 20%) are observed in the pressure field at the blade-tip and root region; however, the global pressure field produces the same total axial force on the disc and turbine. Observation of the second order flow statistics shows that both wakes are characterised by anisotropic fluctuations. More evident anisotropy in the WT wake fluctuations, with higher magnitude in the radial direction, confirms the findings of previous studies. The stronger fluctuations in the WT wake are due to the presence of concentrated tip vortices. These are normally accounted for in the calculation of the *added turbulence* (Lignarolo *et al.*, 2015a). The latter one represents the flow turbulence caused by the presence of the turbine, which is added to the ambient turbulence as explained by Crespo *et al.* (1999) and includes both coherent periodic structures, as the tip-vortices, and random velocity fluctuations, which are not separated in the classical double Reynolds decomposition applied in this work. This leads to the well-known peaks of turbulence intensity close to the rotor at the blade-tip location. However, despite the so-calculated total turbulence intensity in the near wake of the WT is considerably larger than the one in the AD wake (two to four times), both wakes exhibit the same levels of mean-flow kinetic-energy transport in the shear layer, which then collapses to 50% of its original value after the breakdown of the WT tip-vortices after the leapfrogging. This demonstrates how the physics governing the turbulent mixing in the two wakes are intrinsically

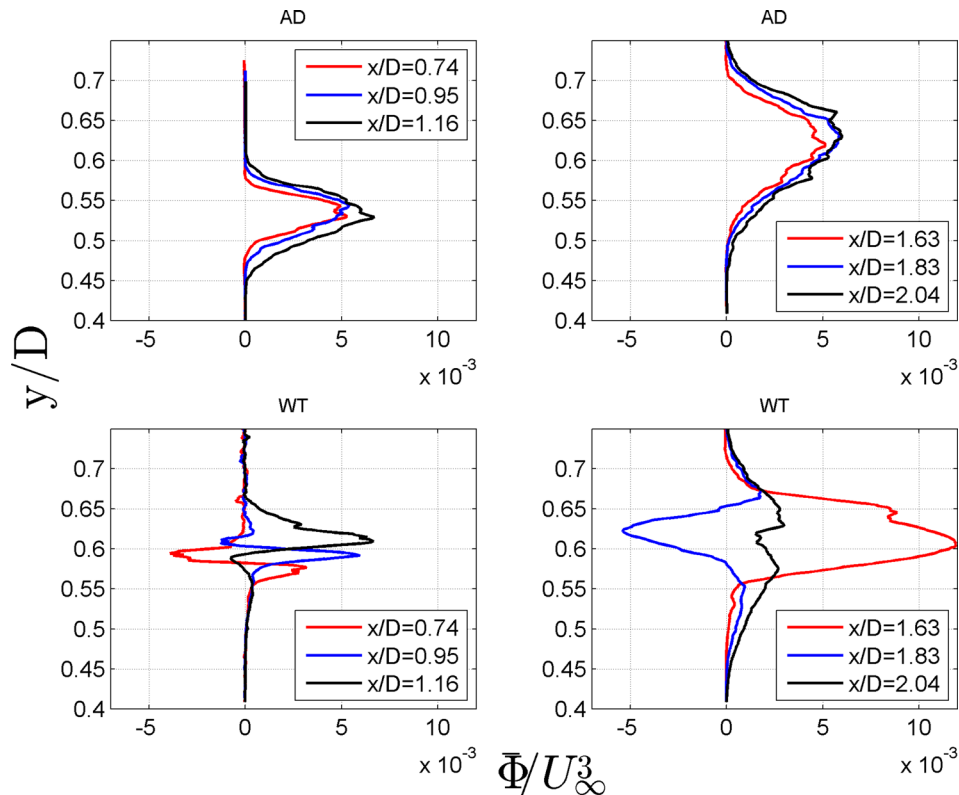


FIG. 23. Mean flow kinetic energy transport at $x/D = 0.95$ and $x/D = 1.83$.

different and, as hypothesised by [Medici \(2005\)](#) and [Lignarolo *et al.* \(2014b\)](#) that the presence of strong coherent fluctuations in the near wake does not enhance the wake mixing. The study has been conducted at low turbulence intensity in order to separate the problems of the flow mixing caused by the external flow fluctuations and the one caused by the turbulence induced directly by the AD or the WT presence. The analysis, as such, showed the intrinsic differences and similarities between the flow in the two wakes, solely due to the wake-induced flow, with no influence of external flow fluctuation, differently from most of the studies on similar subjects, which have been performed in presence of high wind tunnel turbulence or simulated atmospheric boundary layers (and atmospheric turbulence). Our next step in this research will be to perform similar experiments with increased inflow turbulence and analyse the sensitivity of the wake system to the freestream flow fluctuations. In the presence of higher ambient turbulence, as shown by [Ivanell \(2009\)](#), the external flow fluctuations would introduce additional perturbations which would trigger an earlier tip-vortex spiral instability, causing the leapfrogging to move upstream. The method adopted in the present work would still be valid for highlighting the different mixing process characterising the two wakes and, in particular, the influence of the tip-vortex pairing and breakdown. The study has shown that even in the absence of inflow turbulence the velocity fields in the AD and WT wakes are very well comparable, despite the fact that the turbulent mixing is very different. This seems to contradict statements affirming that results from actuator disc simulations are valid only after 5 diameters downstream the disc ([Schepers, 2012](#)). The results suggest the possibility to extend the use of the actuator disc model in numerical simulation until the very near wake, provided that the turbulent mixing is correctly represented.

ACKNOWLEDGMENTS

We would like to acknowledge funding from the FLOW Project. A special thanks to Dr. Gerard Schepers for his collaboration and the provided information.

APPENDIX: STEREO PIV UNCERTAINTY

Measurement uncertainties on the stereo PIV velocity data contain random components, primarily caused by random oscillation of the drive motor rotational frequency, random delays in the triggering systems of the stereo PIV set up, cross-correlation uncertainty, and turbulent fluctuations. The first two sources of uncertainty are considered negligible compared to the others, due to the high-accuracy devices adopted in the present setup. Due to the statistical convergence, the effect of the components due to cross-correlation and flow fluctuations scales with $1/\sqrt{N}$ (with N 200 in the present analysis). For the cross-correlation uncertainty on the vector fields, a typical value of 0.1 pixels on the axial and radial velocity components and 0.2 pixels on the out-of-plane component is expected (Elsinga *et al.*, 2005 and Westerweel, 1993). In this analysis, the method presented by Wieneke (2015) is used for calculating the cross-correlation uncertainty on each instantaneous velocity field and Equation (A1) is used for calculating the uncertainty on the mean values

$$\overline{\varepsilon_u} = \frac{\sqrt{\sum_{i=1}^N (\varepsilon_{u,i})^2}}{N} \quad \overline{\varepsilon_{u'u'}} = \frac{\sqrt{\sum_{i=1}^N (\varepsilon_{u'u',i})^2}}{N}, \quad (\text{A1})$$

respectively, for the time-average velocity and the time-average Reynolds stresses, where ε_u and $\varepsilon_{u'u'}$ are the errors on the single instantaneous SPIV snapshot on the velocity and turbulent fluctuations, respectively: $\varepsilon_{u'u'}$ is calculated with the following equation:

$$\varepsilon_{u'u'} = 2(u - \bar{u})\sqrt{\varepsilon_u^2 - \varepsilon_{\bar{u}}^2}, \quad (\text{A2})$$

which derives from applying the equation of the error propagation (Taylor, 1997) to the $\overline{u'_i u'_i}$ equation. The overall relative uncertainty on the mean velocity due to random components is presented in Table V. A second source of uncertainty of the mean flow properties is related to the limited size of the averaging ensemble, namely, the number of SPIV instantaneous fields. In order to estimate the magnitude of the uncertainty, the relative difference between the flow statistics calculated at 200 samples and the one obtained with 5000 samples has been evaluated. Results are presented in Table V, where the flow is characterized by a negligible vorticity (e.g., free stream and inner wake, excluding the shear layer region), the steady Bernoulli equation can be used to retrieve pressure and the pressure uncertainty is a function of the velocity uncertainty. The former can be estimated from a linear propagation analysis of the Bernoulli equation. The estimation for the pressure uncertainty is reported in Table V. The pressure in the vortical regions is obtained by a second-order Poisson algorithm with potential boundary conditions as explained in Section III B. Because of the relatively well-resolved velocity fields, it can be assumed that the pressure solver keeps the uncertainty on the pressure of the order of the Bernoulli values, as stated by Ragni *et al.* (2014).

TABLE V. Maximum cross-correlation and convergence uncertainty for the mean velocity, Reynolds stresses and pressure.

Quantity	Cross-correlation uncertainty (%)	Convergence uncertainty
\bar{u}	0.15	0.6% (2% in the shear layer)
\bar{v}	2	2%
\bar{w}	1.5	2.5%
$\overline{u'u'}$	3.5	5.5%
$\overline{v'v'}$	0.9	4%
$\overline{w'w'}$	10	13%
\bar{p}	0.1	1%

- Antonia, R. A., Chambers, A. J., Britz, D., and Browne, L. W. B., "Organized structures in a turbulent plane jet: Topology and contribution to momentum and heat transport," *J. Fluid Mech.* **172**, 211–229 (1986).
- Aubrun, S., Devinant, P., and Espana, G., "Physical modelling of the far wake from wind turbines. Application to wind turbine interactions," in European Wind Energy Conference EWEC 2007 (2007).
- Aubrun, S., Loyer, S., Hancock, P. E., and Hayden, P., "Wind turbine wake properties: Comparison between a non-rotating simplified wind turbine model and a rotating model," *J. Wind Eng. Ind. Aerodyn.* **120**, 1–8 (2013).
- Barthelmie, R. J., Rathmann, O., Frandsen, S. T., Hansen, K. S., Politis, E., Prospathopoulos, J., Rados, K., Cabezón, D., Schlez, W., Phillips, J., Neubert, A., Schepers, J. G., and van der Pijl, S. P., "Modelling and measurements of wakes in large wind farms," *J. Phys.: Conf. Ser.* **75**, 012049 (2007).
- Batchelor, G. K., *An Introduction to Fluid Dynamics* (Cambridge University Press, 2000).
- Batchelor, G. K. and Townsend, A. A., "Decay of vorticity in isotropic turbulence," *Proc. R. Soc. London. Ser. A* **190**, 534–550 (1947).
- Batchelor, G. K. and Townsend, A. A., "Decay of isotropic turbulence in the initial period," *Proc. R. Soc. London. Ser. A* **193**, 539–558 (1948a).
- Batchelor, G. K. and Townsend, A. A., "Decay of turbulence in the final period," *Proc. R. Soc. London. Ser. A* **194**, 527–543 (1948b).
- Bolnot, H., Le Dizès, S., and Leweke, T., "Wind energy—impact of turbulence," in *Pairing Instability in Helical Vortices* (Springer Berlin Heidelberg, 2014), pp. 23–28.
- Bolnot, H., Leweke, T., and Le Dizes, S., "Spatio-temporal development of the pairing instability in helical vortices," in 6th AIAA Theoretical Fluid Mechanics Conference (American Institute of Aeronautics and Astronautics, Inc., 2011).
- Burton, T., Sharpe, D., Jenkins, N., and Bossanyi, E., *Wind Energy Handbook* (John Wiley & Sons, 2001).
- Cal, R. B., Lebrón, J., Castillo, L., Kang, H. S., and Meneveau, C., "Experimental study of the horizontally averaged flow structure in a model wind-turbine array boundary layer," *J. Renewable Sustainable Energy* **2**, 013106 (2010).
- Calaf, M., Meneveau, C., and Meyers, J., "Large eddy simulation study of fully developed wind-turbine array boundary layers," *Phys. Fluids* **22**, 015110 (2010).
- Cantwell, B. and Coles, D., "An experimental study of entrainment and transport in the turbulent near wake of a circular cylinder," *J. Fluid Mech.* **136**, 321–374 (1983).
- Chamorro, L. P., Arndt, R. E. A., and Sotiropoulos, F., "Reynolds number dependence of turbulence statistics in the wake of wind turbines," *Wind Energy* **15**, 733–742 (2012).
- Chen, T. Y. and Liou, L. R., "Blockage corrections in wind tunnel tests of small horizontal-axis wind turbines," *Exp. Therm. Fluid Sci.* **35**, 565–569 (2011).
- Cotroni, A., Di Felice, F., Romano, G. P., and Elefante, M., "Investigation of the near wake of a propeller using particle image velocimetry," *Exp. Fluids* **29**, S227–S236 (2000).
- Crespo, A., Hernández, J., and Frandsen, S., "Survey of modelling methods for wind turbine wakes and wind farms," *Wind Energy* **2**, 1–24 (1999).
- Dobrev, I., Maalouf, B., Troldborg, N., and Massouh, F., "Investigation of the wind turbine vortex structure," in 14th International Symposium on Applications of Laser Techniques to Fluid Mechanics (2008).
- El Kasmi, A. and Masson, C., "An extended model for turbulent flow through horizontal-axis wind turbines," *J. Wind Eng. Ind. Aerodyn.* **96**, 103–122 (2008).
- Elsinga, G. E., van Oudheusden, B. W., and Scarano, F., "Evaluation of aero-optical distortion effects in PIV," *Exp. Fluids* **39**, 246–256 (2005).
- Escudé, R. and Liné, A., "Experimental analysis of hydrodynamics in a radially agitated tank," *AICHE J.* **49**, 585–603 (2003).
- Felli, M., Camussi, R., and Di Felice F., "Mechanisms of evolution of the propeller wake in the transition and far fields," *J. Fluid Mech.* **682**, 5–53 (2011).
- Gaumond, M., Rethore, P. E., Bechmann, A., Ott, S., Larsen, G. C., Peña, A., and Hansen, K. S., "Benchmarking of wind turbine wake models in large offshore windfarms," in Science of Making Torque from Wind (2012).
- Hamilton, N., Kang, H. S., Meneveau, C., and Cal, R. B., "Statistical analysis of kinetic energy entrainment in a model wind turbine array boundary layer," *J. Renewable Sustainable Energy* **4**, 063105–063119 (2012).
- Hussain, A. K. M. F., "Coherent structures—reality and myth," *Phys. Fluids* **26**, 2816–2850 (1983).
- Ivanell, S., "Numerical computations of wind turbine wakes," Linne Flow Centre, Department of Mechanics, Royal Institute of Technology KTH—Gotland University, Stockholm, Sweden, 2009.
- Ivanell, S., Mikkelsen, R., Sørensen, J. N., and Henningson, D., "Stability analysis of the tip vortices of a wind turbine," *Wind Energy* **13**, 705–715 (2010).
- Leweke, T., Bolnot, H., Quaranta, U., and Le Dizes, S., "Local and global pairing in helical vortex systems," in International Conference on Aerodynamics of Offshore Wind Energy Systems and Wakes (2013).
- Lignarolo, L. E. M., Ragni, D., Krishnaswami, C., Chen, Q., Simão Ferreira, C. J., and van Bussel, G. J. W., "Experimental analysis of the wake of a horizontal-axis wind-turbine model," *Renewable Energy* **70**, 31–46 (2014a).
- Lignarolo, L. E. M., Ragni, D., Scarano, F., Simao Ferreira, C. J., and van Bussel, G. J. W., "Tip vortex instability and turbulent mixing in wind turbine wakes," *J. Fluid Mech.* **781**, 467–493 (2015a).
- Lignarolo, L. E. M., Ragni, D., Simão Ferreira, C., and van Bussel, G. J. W., "Kinetic energy entrainment in wind turbine and actuator disc wakes: An experimental analysis," *J. Phys.: Conf. Ser.* **524**, 012163 (2014b).
- Lignarolo, L. E. M., Ragni, D., Simao Ferreira, C. J., and van Bussel, G. J. W., "Turbulent mixing in wind turbine and actuator disc wakes: Experiments and POD analysis," 33rd ASME Wind Energy Symposium (American Institute of Aeronautics and Astronautics, 2015b).
- Liu, X. and Katz, J., "Instantaneous pressure and material acceleration measurements using a four-exposure PIV system," *Exp. Fluids* **41**, 227–240 (2006).
- Medici, D., *Experimental Studies of Wind Turbine Wakes—Power Optimisation and Meandering, Mechanics* (Royal Institute of Technology (KTH), Stockholm, 2005).
- Meyers, J. and Meneveau, C., "Optimal turbine spacing in fully developed wind farm boundary layers," *Wind Energy* **15**, 305–317 (2012).

- Mikkelsen, R., "Actuator disc methods applied to wind turbines," Department of Mechanical Engineering, Technical University of Denmark, Denmark, 2003.
- Nishino, T. and Willden, R. H. J., "Effects of 3-D channel blockage and turbulent wake mixing on the limit of power extraction by tidal turbines," *Int. J. Heat Fluid Flow* **37**, 123–135 (2012).
- Odemark, Y. and Fransson, J. H. M., "The stability and development of tip and root vortices behind a model wind turbine," *Exp. Fluids* **54**, 1–16 (2013).
- Pierella, F. and Sætran, L. R., "Effect of initial conditions on flow past grids of finite extension," in 17th Australasian Fluid Mechanics Conference (2010).
- Raffel, M., Willert, C. E., and Kompenhans, J., *Particle Image Velocimetry: A Practical Guide (with 24 Tables)* (Springer-Verlag GmbH, 1998).
- Ragni, D., Oudheusden, B. W., and Scarano, F., "Non-intrusive aerodynamic loads analysis of an aircraft propeller blade," *Exp. Fluids* **51**, 361–371 (2011).
- Ragni, D., Oudheusden, B. W., and Scarano, F., "3D pressure imaging of an aircraft propeller blade-tip flow by phase-locked stereoscopic PIV," *Exp. Fluids* **52**, 463–477 (2012).
- Ragni, D., Simao Ferreira, C. J., and Correale, G., "Experimental investigation of an optimized airfoil for vertical-axis wind turbines," *Wind Energy* **18**, 1629 (2014).
- Reynolds, W. C. and Hussain, A. K. M. F., "The mechanics of an organized wave in turbulent shear flow. Part 3. Theoretical models and comparisons with experiments," *J. Fluid Mech.* **54**, 263–288 (1972).
- Sanderse, B., van der Pijl, S. P., and Koren, B., "Review of computational fluid dynamics for wind turbine wake aerodynamics," *Wind Energy* **14**, 799–811 (2011).
- Sanz Rodrigo, J. and Moriarty, P., "TASK 31—Benchmarking of wind farm flow models," Final Report to ExCo 74, Prince Edward Island, Canada, 2014.
- Schepers, J. G., *Engineering models in wind energy aerodynamics, Aerospace Engineering* (Delft University of Technology, 2012).
- Schreck, S. J., Sørensen, N. N., and Robinson, M. C., "Aerodynamic structures and processes in rotationally augmented flow fields," *Wind Energy* **10**, 159–178 (2007).
- Schümann, H., Pierella, F., and Sætran, L., "Experimental investigation of wind turbine wakes in the wind tunnel," *Energy Procedia* **35**, 285–296 (2013).
- Selig, M. S., Guglielmo, J. J., Broeren, A. P., and Giguère, P., *Summary of Low-Speed Airfoil Data* (SoarTech Publications, Virginia Beach, VA, 1995).
- Sforza, P. M., Sheerin, P., and Smorto, M., "Three-dimensional wakes of simulated wind turbines," *AIAA J.* **19**, 1101–1107 (1981).
- Sherry, M., Sheridan, J., and Lo Jacono, D., "Horizontal axis wind turbine tip and root vortex measurements," in 15th International Symposium on Applications of Laser Techniques to Fluid Mechanics (2010).
- Taylor, J. R., *An Introduction to Error Analysis: The Study of Uncertainties in Physical Measurements* (University Science Books, 1997).
- van Oudheusden, B. W., "PIV-based pressure measurement," *Meas. Sci. Technol.* **24**, 032001 (2013).
- Vermeer, L. J., Sørensen, J. N., and Crespo, A., "Wind turbine wake aerodynamics," *Prog. Aerosp. Sci.* **39**, 467–510 (2003).
- Westerweel, J., *Digital Particle Image Velocimetry, Mechanical Maritime and Materials Engineering* (Delft University of Technology, Delft, 1993).
- Westerweel, J., "Fundamentals of digital particle image velocimetry," *Meas. Sci. Technol.* **8**, 1379–1392 (1997).
- Whale, J., Anderson, C. G., Bareiss, R., and Wagner, S., "An experimental and numerical study of the vortex structure in the wake of a wind turbine," *J. Wind Eng. Ind. Aerodyn.* **84**, 1–21 (2000).
- Wieneke, B., "PIV uncertainty quantification from correlation statistics," *Meas. Sci. Technol.* **26**, 074002 (2015).
- Wu, Y. T. and Porté-Agel, F., "Large-Eddy simulation of wind-turbine wakes: evaluation of turbine parametrisations," *Boundary-Layer Meteorol.* **138**, 345–366 (2011).